Experiments in Fluids 32 (2002) 533–541 © Springer-Verlag 2002
DOI 10.1007/s00348-001-0373-8

Influence of the optical configuration on temperature measurements with fluid-dispersed TLCs

A. Günther, Ph. Rudolf von Rohr

Abstract An accurate temperature calibration of fluid-dispersed thermochromic liquid crystal (TLC) particles is an important prerequisite for quantitative liquid crystal thermometry (LCT) measurements in flows. Encapsulated TLCs are subjected to uniform and linear temperature fields and are illuminated with a sheet of white light. A digital camera records the color distribution reflected by the particles. For the first time, a telecentric objective is used to eliminate the angular dependence of the color within the image plane.

The paper systematically assesses how the temperature calibration is affected by the angle between the camera axis and the light-sheet plane, and by the properties of the working fluid. The obtained results provide design criteria for quantitative LCT measurements in situations where small spatial variations of the fluid temperature need to be resolved, namely for turbulent heat transfer problems in wall-bounded flows.

Symbols

AOV	area of view (m^2)
C	coefficient of polynomial (–)
d_p, d_e	particle diameter and particle image diameter (m)
d_r	length of a square pixel (m)
f	focal length (m)
$f_\#$	f-number of the camera objective (–)
h	distance between two walls (m)
H	hue, H:[0, 2π] (rad)
i, j	pixel counters; i: [1, 768] (x-direction); j: [1, 572] (y-direction)
I	intensity, I: [0, 255]
k, l	counters for calculating local averages; k: [1, N_k] (x-direction); j: [1, N_k] (y-direction)
m	number of (locally averaged) temperature locations in the horizontal direction of a rectangular 2-D domain (–)
M	magnification factor (–)
n	number of (locally averaged) temperature locations in the vertical direction of a rectangular 2-D domain (–), refractive index (–)
R, G, B	red, green, blue intensities, R, G, B: [0, 255]
S	saturation, S: [0, 255]
t	time (s)
t_{resp}	response time (s)
T	Celsius temperature (°C); thermodynamic temperature (K)
$T_{S,nom}$	nominal start of temperature sensitivity range (°C)
T	linear transformation
u_s	settling velocity
v_1, v_2	functions of R, G, B
x, y, z	Eulerian Cartesian coordinates (m)
β	volumetric thermal expansion coefficient (1/K)
δ	uncertainty calculated for $\pm 2\sigma$ (95.4% confidence)
δ_{LS}	light sheet thickness (m)
δ_{tel}	telecentric range (m)
δ_z	depth of field (m)
η	exponent of polynomial
ϕ	angle between light-sheet plane and camera axis (°)
Φ	post-processing path
κ	thermal diffusivity (m^2/s)
λ	wavelength (m), thermal conductivity (W/mK)
ρ	density (kg/m^3)
ν	kinematic viscosity (m^2/s)
σ	standard deviation
ξ	index running over time (–)

Abbreviations

CCD	charge-coupled device
CT	color temperature
LCT	liquid crystal thermometry
PAL	phase-alternating line, video standard
PIV	particle image velocimetry
PIV/T	particle image velocimetry/thermometry
PMMA	polymethyl methacrylate
RAM	random access memory
WB	white light balance
2-D	two-dimensional

Subscripts and superscripts

G	glycerol
L	lower wall
mean	mean value

Received: 22 January 2001/Accepted: 16 October 2001

A. Günther (✉), Ph. Rudolf von Rohr
Institute of Process Engineering
Swiss Federal Institute of Technology (ETH) Zurich
8092 Zürich, Switzerland
e-mail: vonrohr@ivuk.mavt.ethz.ch

The involvement of Eric Ammann, Andreas Berger, and Martin Thommen in conducting the experiments is highly appreciated. Christopher Rowland (Hallcrest) provided the TLC material together with detailed information on its physical properties. We thank Dr. Arno Laesecke, National Institute of Standards and Technology (NIST) Boulder, U.S.A., for his advice concerning the fluid properties of glycerol–water solutions. The support provided by Sony Overseas, Foba, Volpi, Visual Solutions, Stemmer Imaging, and Sill Optics is gratefully acknowledged.

min	minimum value
U	upper wall
poly	polynomial
p	particle
set	settling
W	water

1 Introduction

Unlike the case for measuring two-dimensional (2-D) velocity fields, few techniques are available that provide information for the whole field for fluid temperatures. Commonly used techniques are liquid crystal thermometry/thermography (LCT) and laser-induced fluorescence (LIF). A two-color LIF technique, which relates the temperature to an intensity ratio of wavelengths reflected by two dyes, was recently reported by Sakakibara and Adrian (1999). The main advantage of LCT is that the temperature sensitivity range as well as its starting temperature can be adjusted in a wide range through modifying the LC formulation. Furthermore, for postprocessing of LCT measurements, it is common practice that the local fluid temperature is related to a ratio of the (multiple) intensity signals collected at different frequency bands. This is advantageous, since the effect of local intensity variations of the illuminating light does not necessarily result in poorly predicted local fluid temperatures.

When suspended in a transparent fluid, encapsulated thermochromic liquid crystals[1] change their color as a function of the local fluid temperature. We consider an experimental configuration for the LCT technique that allows combination with particle image velocimetry (PIV) in order to provide simultaneous temperature and velocity measurements in transient flow situations. Figure 1 illustrates the two paths for reconstructing the velocity Φ_1 and the temperature field Φ_2. Applications of the LCT technique based on fluid-dispersed TLCs are reported by Dabiri and Gharib (1996, 1991), Kasagi et al. (1989), Park et al. (2001), and Smith et al. (2001), and focus on natural convection problems, flows around bluff bodies, and free shear flows. In this paper we will see that the small effective temperature sensitivity range of the LCT technique is particularly advantageous for turbulent heat transfer studies in wall-bounded flows (Günther 2001).

In most previous studies the particle image diameters were smaller than the size of one CCD pixel, which is not disadvantageous for measuring fluid temperatures, but restricts the accuracy of simultaneously obtaining the velocity prediction through local cross-correlation of subsequent digital images (Adrian 1995). For the measurements presented in this paper, the digital particle images are represented by more than one pixel and therefore provide the spatial resolution required to prevent peak locking. This paper exclusively focuses on the temperature calibration in a thermally stratified fluid layer, a prerequisite for path Φ_2. In Sect. 2, we present an optical setup in which the angle between light sheet and camera axis, the working fluid, and the influence of the white light balance (WB) of the light source and the camera can be varied. Image-processing and calibration procedures are described in Sects. 3 and 4. The influence of the optical configuration on the temperature calibration is discussed in Sect. 5.

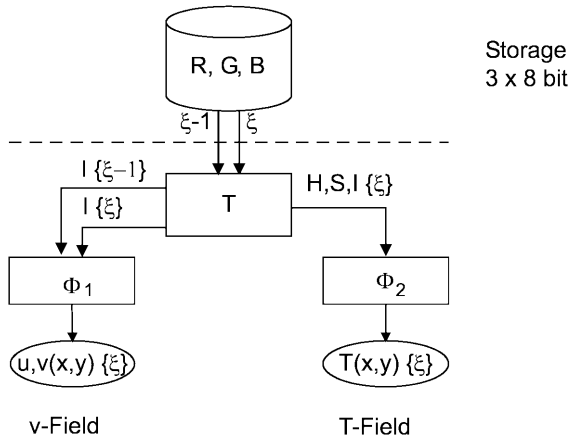

Fig. 1. Postprocessing of the stored image files for obtaining 2-D velocity (Φ_1) and temperature fields (Φ_2)

2 Experimental

Figure 2 shows a schematic of the experimental setup. Measurements are conducted in a cylindrical fluid-filled cavity. The rectangular bottom and top walls have the dimensions 300 mm × 150 mm. The horizontal walls are separated by 24 mm in the vertical direction and consist of two parallel black-anodized aluminum bodies. The wall temperatures – T_L at the bottom and T_U at the top wall – are adjusted by two independent constant-temperature water baths. The transparent cylinder is located between the walls, has an inner diameter of 100 mm and a wall thickness of 5 mm, and is made of PMMA (polymethyl methacrylate, $\lambda = 0.21$ W/mK) material. A rectangular section of the cylinder, located adjacent to the camera, is replaced by a flat window of the same material, see Fig. 3. The entire box is insulated by a 50-mm thermal shield. The insulation is only partially removed during image acquisition in order to provide optical access. Approximately 0.03 vol.% of the TLC slurry (Hallcrest, BM/R35C20 W) is added to the transparent working fluid in the cylindrical cavity, either de-ionized water or glycerol. In order to make the technique applicable to measurements in turbulent flow situations, encapsulated TLCs with a relatively small particle diameter of 19.75 μm and a standard deviation of 7.18 μm were used. The particle size was measured in aqueous suspension using laser light diffraction (Sympatec). The thermal diffusivity α_p of encapsulated TLCs is $5.8 \cdot 10^{-8}$ m^2/s (Dabiri and Gharib 1991). According to Hallcrest (1999), a typical value of the overall particle density ρ_p is 1020 kg/m^3, where the density of the TLC core varies between 970 kg/m^3 and 1010 kg/m^3 depending on the composition. The wall material, which consists of gelatin, gum arabic, and water, has a density of approximately 1100 kg/m^3. From these quantities a thermal response time of 1 ms can be estimated. In Table 1, the experimental configuration is summarized and compared with previous heat transfer studies

[1] We use the term "TLC particles" in the following.

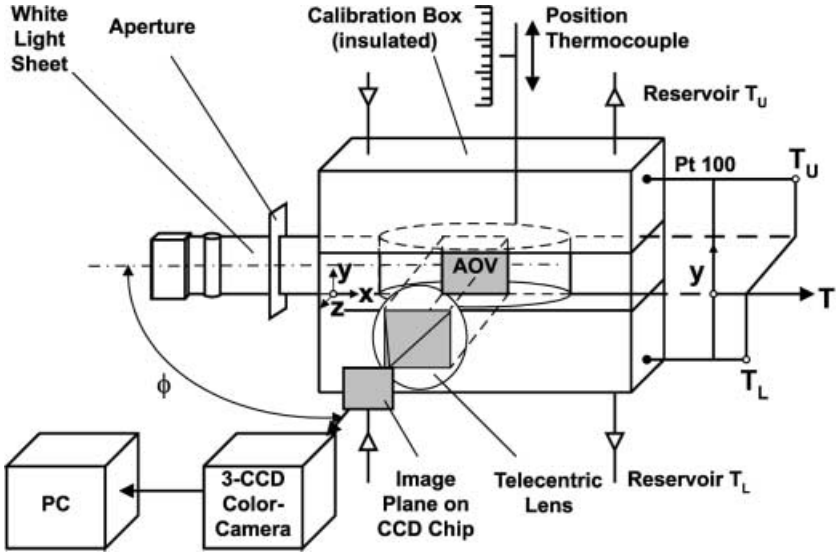

Fig. 2. Experimental configuration with the fluid-filled cavity between an isothermal bottom (T_L) and top surface (T_U), the light-sheet plane, and the CCD camera with telecentric lens. The temperature profile is shown for a thermally stratified layer

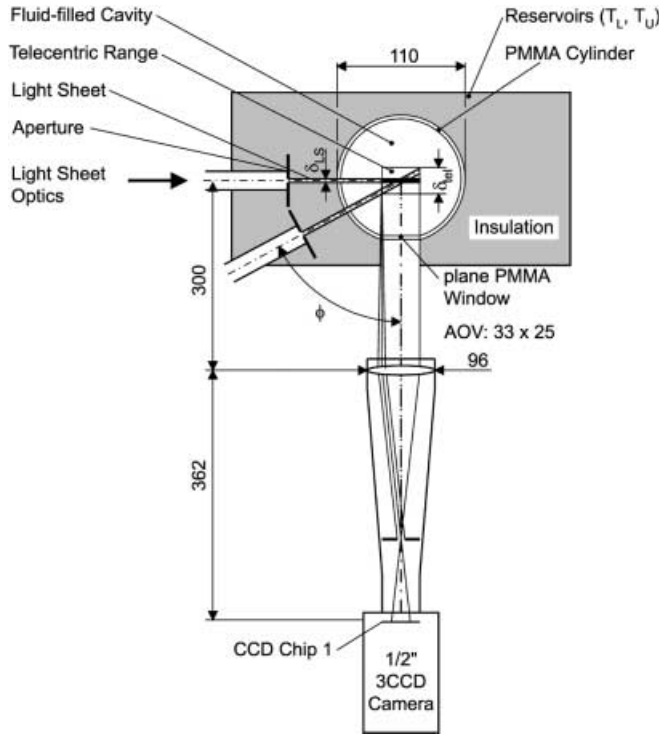

Fig. 3. Optical configuration with the insulated cylindrical cavity. The angle ϕ between the light-sheet plane and the axis of the telecentric objective is variable (distances in mm)

in an impinging jet (Dabiri and Gharib 1991), around a heated cylinder (Park et al. 2001), and in a cubic cavity that is heated from below (Lutjen et al. 1999).

A magnetic stirrer is located inside the cavity and is used to mix the fluid during constant temperature measurements as well as to prevent the particles from settling. Inside the cavity, the temperature is measured with a reference resistance thermometer (Pt, 100 Ω), which was calibrated according to ITS-90 and has a measurement uncertainty of 0.03 °C for the considered temperature range. In addition, a thermocouple allows the local temperature to be measured at variable distances y from the bottom wall. A 90-W metal halide light source (Volpi, model Intralux IWL500e) with the color temperature of 5500 K ± 900 K is used. The light is guided through a fiber-optic line converter (Volpi, model VVLC), where a continuous sheet of white light is produced. A cylindrical lens and an aperture adjust the light-sheet thickness to approximately $\delta_{LS} = 1$ mm. The light sheet illuminates the TLC particles in a vertical plane between the two walls. A progressive-scan 3-chip video camera (Sony, model DXC-9100P) is positioned with its optical axis perpendicular ($\phi = 90°$) to the light sheet plane. The WB of the camera can be manually altered. To exclude the dependence of the recorded color information on the viewing angle within the area of view, the camera is equipped with a telecentric objective (Sill Imaging, Germany), which is focused on the light sheet, see Fig. 3. The objective has a magnification

Table 1. Comparison of experimental parameters

Parameter	LCT	PIV/T	LCT	PIV/T
	Dabiri and Gharib (1991)	Park et al. (2001)	Lutjen et al. (1999)	Present study
Area of view (AOV)	163 × 120 mm^2	60 × 50 mm^2	≈ 76 × 57 mm^2	35 × 35 mm^2
Mean diameter d_p	150 μm	40 μm	40 μm	19.75 μm
Response time t_{resp}	60 ms	4 ms	4 ms	1 ms
Magn. factor M	≈0.04	0.11	≈ 0.084	0.19
Fluid	Water	Water	Glycerol	Water/glycerol

factor M of 0.19, an area of view (AOV) of 33 mm × 25 mm, and a working distance of 300 mm.

Spherical TLC particles, located in the light-sheet plane, are illuminated with white light. A fraction of the light is scattered at the particle surfaces. In contrast to a standard PIV configuration, the influence of scattered light, which for given particle properties depends on the fluid's refractive index n, is unwanted. The desired information is a band of dominant wavelengths that is reflected from the TLC particles as a function of the local fluid temperature. The three CCD chips of the camera (768 × 572 pixels) transiently record separate color bands of the reflected light as analog RGB information. The size of one square pixel is 8.3 × 8.3 μm^2. With a 4-MB dual-ported memory framegrabber board (ITI model IC4-RGB), the images are digitized and downloaded to the RAM (128 MB) of a personal computer, where the commercial software package Optimas 6.5 (Media Cybernetics) is used for image acquisition.

3 Image processing and optical resolution

Camera images are downloaded into the computer RAM and subsequently stored as RGB files (3 × 8 bit) in the .TIFF format at a local hard disk. Even though postprocessing starts with the digitized images, it is important to note that the recorded RGB information not only depends on the angle of illumination but also on the WB between the three chips. Only a fixed WB enables us to obtain quantitative results from the recorded RGB intensities. For a known temperature calibration, such information can then be used for simultaneously obtaining temperature and velocity in transient flows. Temperature and velocity are obtained by two postprocessing steps Φ_1 and Φ_2 from the transiently recorded RGB images, see Fig. 1.

Even though this paper does not focus on the reconstruction of the velocity fields, path Φ_1 in Fig. 1, we first want to demonstrate that the particle image diameter for the considered configuration is sufficient for performing combined LCT and PIV measurements in transient flow situations. The intensities I_{ij} of two subsequent images, which are recorded at the times t_ζ and $t_{\zeta+1}$, are locally cross-correlated. Standard PIV algorithms use three-point estimators to fit the discrete correlation data and to predict the displacement at a sub-pixel level. The uncertainty of the velocity prediction depends on the particle image diameter d_e (Raffel et al. 1998) and can be reduced if a particle image is represented by more than one pixel on the camera chip. In the following, we estimate the average number of pixels by which a TLC particle is represented on the chip. For diffraction-limited imaging, the particle image diameter can be obtained (Adrian 1995) from:

$$d_e = \sqrt{\left(Md_\mathrm{p}\right)^2 + \left(2.44 f_\# (M+1)\lambda\right)^2} \quad , \tag{1}$$

with the magnification factor M and the mean particle diameter d_p where $f_\#$ characterizes the aperture of the camera objective. In Table 2, the calculated particle image diameters as well as the depth of field (Adrian 1995),

$$\delta_z = 4.88\lambda\left[f_\#\left(1+\frac{1}{M}\right)\right]^2 \quad , \tag{2}$$

Table 2. Particle image diameter and depth of field for diffraction-limited imaging

$f_\#$	d_e/d_r (470–630 nm)	δ_z (470–630 nm)
1.6	0.52–0.57	0.23–0.31 mm
2.8	0.64–0.77	0.72–0.96 mm
4.0	0.80–0.99	1.5–2.0 mm
5.6	1.0–1.3	2.9–3.9 mm
8.0	1.4–1.8	5.9–7.9 mm
11	1.9–2.5	11–15 mm
16	2.7–3.6	23–31 mm

are listed for wavelengths between $\lambda_1 = 470$ nm (blue) and $\lambda_2 = 630$ nm (red) as a function of $f_\#$. Satisfying $d_e/d_r > 1$ and using the full telecentric range δ_{tel} of the objective, 15 mm, therefore implies a minimum $f_\#$ of 11. This is not a restriction since we consider uniform or linear temperature fields in this paper. For transient flows, however, higher-energy (pulsed) light sources might be required, depending on the characteristic velocity of the flow.

We now discuss how temperature fields are related to the RGB images, path Φ_2 in Fig. 1. As commonly done in the literature, we perform a linear transformation with the red R_{ij}, the green G_{ij}, and the blue intensities B_{ij} in the image plane $i: 1,\ldots,768$ and $j: 1,\ldots,572$ (Dabiri and Gharib 1991; Farina et al. 1994):

$$\begin{bmatrix} \upsilon_{1,ij} \\ \upsilon_{2,ij} \\ I_{ij} \end{bmatrix} = \begin{bmatrix} 2/\sqrt{6} & -1/\sqrt{6} & -1/\sqrt{6} \\ 0 & 1/\sqrt{6} & -1/\sqrt{6} \\ 1/3 & 1/3 & 1/3 \end{bmatrix} \cdot \begin{bmatrix} R_{ij} \\ G_{ij} \\ B_{ij} \end{bmatrix} \quad , \tag{3}$$

where the third component of the vector on the left represents the local intensity $\boldsymbol{I}_{ij}$. The local hue H_{ij} and the saturation S_{ij} are obtained as follows:

$$H_{i,j} = \begin{cases} \pi/2 - \tan^{-1}\left(\boldsymbol{\upsilon}_{1,ij}/\boldsymbol{\upsilon}_{2,ij}\right) : B_{ij} < G_{ij}, \\ \pi/2 + \tan^{-1}\left(\boldsymbol{\upsilon}_{1,ij}/\boldsymbol{\upsilon}_{2,ij}\right) : B_{ij} \geq G_{ij} \end{cases} , \tag{4}$$

$$S_{ij} = \sqrt{\upsilon_{1,ij}^2 + \upsilon_{2,ij}^2} \quad . \tag{5}$$

In the considered color system, H_{ij} defines an angle in the interval $[0, 2\pi]$. Three criteria are defined

- $I_{ij} > \langle I\rangle_{ij}$, $\langle I\rangle_{ij}$ denotes an average over all pixels
- R_{ij} or G_{ij} or $B_{ij} < 255$
- $S_{ij} > S_{\min}$

The first criterion excludes low-intensity background light (underflow) and ensures that the color information is obtained from TLC particles only. The second criterion disregards saturated pixels (overflow). The purpose of the third criterion is to further minimize the contribution of white light. Only pixels that fulfill all criteria are considered. From the validated hues H_{ij} local averages H_{kl} are calculated. In this paper, we consider $k: 1,\ldots,m$ and $l: 1,\ldots,n$ with $m = n = 40$, and a spot size of 32 × 32 pixels. It is assumed a relation $T_{kl} = f(H_{kl})$ can be obtained in known temperature fields. The calibration curve, the measurement accuracy, and the influence of the experimental configuration on the calibration are discussed in the following sections.

4 Calibration

A number of papers describe the temperature calibration for encapsulated TLCs (e.g. Hay and Hollingsworth 1998). However, mostly encapsulated TLCs are appliqued on a constant temperature surface, where the location of the camera axis is close to the direction of illumination (small ϕ). Behle et al. (1996) studied the dependence of the calibration of liquid crystal sheets on the angle between the direction of illumination and observation. For the calibration of TLCs in a fluid with $\phi = 90°$, a thermally stratified fluid layer can be used (e.g. Günther and Rudolf von Rohr 2000) where the bottom wall of the cavity is cooled, the top wall is heated, and the side walls are thermally insulated.

The TLC slurry is dispersed in the working fluid. To ensure that particles are homogeneously distributed and to avoid particle agglomeration and the formation of air bubbles at wall surfaces, the suspension of TLC particles in the working fluid is heated to 70 °C and then subjected to an ultrasound bath prior to filling it into the cavity.

At the low end of the temperature sensitivity range, TLC particles reflect a red color. With increasing temperatures, green and subsequently blue become the dominant colors. Since the color response depends on the illumination angle (Kasagi et al. 1989), and the directions of illumination and observation do not coincide for light sheet applications, the "effective" temperature sensitivity range is significantly reduced compared to its nominal value ($\phi = 0°$) of approximately 20 °C. In this section we use the angle $\phi = 90°$ for the calibration, a configuration that is most relevant to light sheet measurements. The angular dependence of the results is discussed in Sect. 5.2. The calibration is carried out in a uniform and a linear (thermally stratified layer) temperature field.

4.1 Thermally stratified layer

A thermally stratified layer is desired because the calibration can be reduced to one single measurement. However, it is only feasible if (a) the vertical temperature in the fluid is linear, i.e. the side walls are well insulated, and (b) the TLC particles are not settled before the linear profile is developed.

Linearity. After the horizontal aluminum walls reach the constant temperatures T_L and T_U, the suspension of TLC particles and deionized water is mixed with a magnetic stirrer. After stirring, the linear temperature profile develops through thermal conduction. Thermocouple measurements of the vertical temperature profile of the thermally stratified layer confirmed its linearity. The measurement uncertainty was minimized by using a relatively large temperature difference of 10 °C. Assuming constant fluid properties, the necessary time t to develop the linear profile can be estimated by solving the conduction equation,

$$\frac{\delta T}{\delta t} = \kappa \frac{\delta^2 T}{\delta y^2} \quad , \tag{6}$$

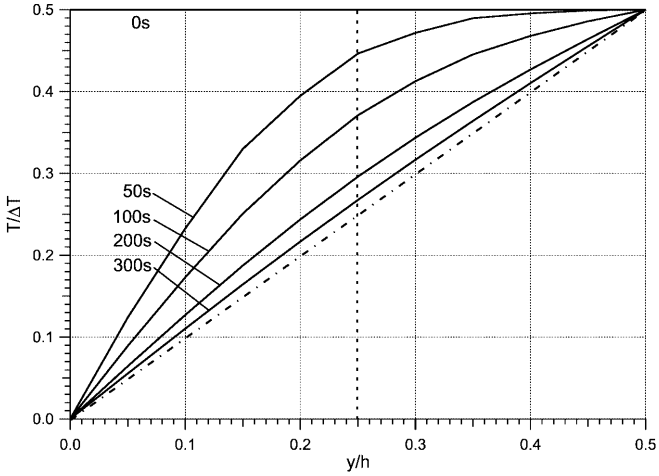

Fig. 4. Transient development of the temperature profile in the lower half of the water layer

for the initial condition $T(t = 0, y/h) = 0.5(T_L + T_U)$ and the boundary conditions $T(t, y/h = 0) = T_L$ and $T(t, y/h = 1) = T_U$. For different instants in time, the numerically obtained temperature profiles are plotted in Fig. 4 for a 25-mm layer of water. Only the lower half is shown, since deviation of the obtained profiles from the linear profile is a point-symmetric function with respect to the center of the layer. Figure 5 shows the relative deviation between the instantaneous fluid temperature $T(t, y/h = 0.25)$ and the developed linear profile $T\langle t \to \infty, y/h = 0.25\rangle$ versus time. The thermal diffusivities κ are 0.150×10^{-6} m^2/s for water and 0.914×10^{-7} m^2/s for glycerol.

Particle settling. The influence of particle sedimentation is shown in the same diagram. Assuming Stokes flow, the effect of settling can be obtained from the linear relation

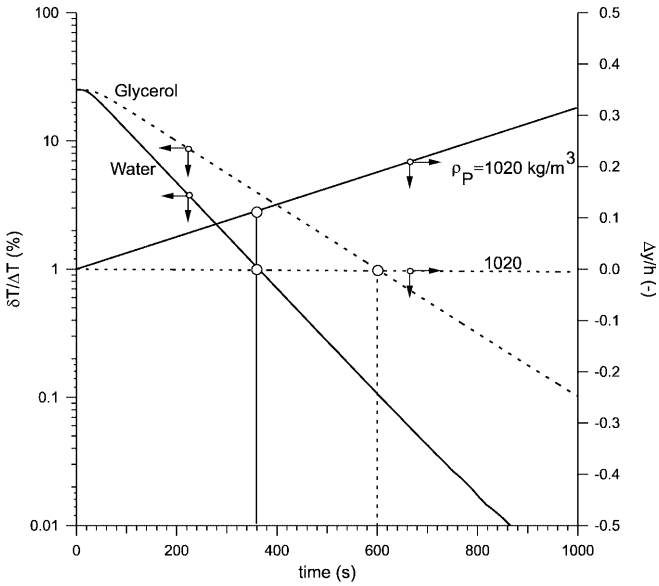

Fig. 5. *Left axis*: relative difference between the developing temperature profile and the linear limit versus time at $y/h = 0.25$ for water (*solid line*) and glycerol (*dashed line*). *Right axis*: influence of sedimentation of particles with the overall density of 1020 kg/m^3 in the two fluids

Table 3. Fluid properties of water and glycerol at T_b = 35 °C (Wagner and Kruse 1998; D'Ans et al. 1977)

Fluid property	Water	Glycerol
Kinematic viscosity ν (m^2/s)	0.724×10^{-6}	0.371×10^{-3}
Density ρ (kg/m^3)	994	1250
Thermal conductivity λ (W/K m)	0.623	0.281
Thermal diffusivity κ (m^2/s)	0.150×10^{-6}	0.914×10^{-7}
Prandtl number Pr	4.82	4060
Vol. thermal expansion coefficient β (1/K)	3.46×10^{-4}	6.10×10^{-4}
Heat capacity c_p (kJ/kg K)	4.18	2.45
Refractive index n (–)	1.33	1.47

$$\frac{\Delta y(t)}{h} = \frac{d_p^2 g t}{18 \nu h} \cdot \left(\frac{\varrho_p}{\varrho} - 1 \right) \ , \tag{7}$$

where ρ_p is the overall particle density, 1020 kg/m^3 (Hallcrest 1999), d_p is the mean particle diameter, and g denotes the gravitational acceleration. The density ρ and the kinematic viscosity ν of the fluids are summarized in Table 3. Positive values of $\Delta y/h$ indicate a downward motion of the particles, while negative values indicate an upward motion. For the water layer (solid lines), it takes about 6 min until the deviation from the linear profile is smaller than 1% of the temperature drop across the layer, resulting in a distance $\Delta y/h$ equal to 11% of the layer depth. The corresponding time for glycerol (dashed lines) is 10 min, during which the TLC particles only pass 0.2% of the layer depth for the considered particle density.

In Fig. 6 the line averages of the hue $\langle H_{kl} \rangle_k$ the saturation $\langle S_{kl} \rangle_k$ and the intensity $\langle I_{kl} \rangle_k$ are plotted versus the linear temperature profile. The temperatures at the bottom wall, 33.61 °C, and at the top wall, 35.37 °C, are obtained from resistance thermometer readings. The uncertainties for $\langle H_{kl} \rangle_k$ are plotted for a confidence interval of 95.4% (twice the standard deviation). Small hues correspond to low fluid temperatures. The nonlinear character of the calibration should be noted. Calibration in a linear temperature field allows us to accurately resolve the steep gradient at the beginning of the temperature sensitive range. The saturation is large at low fluid temperatures and decreases for increasing hues. One important result is that for hue values within the temperature sensitivity range, the relation $T \rightarrow H$ is unequivocal. Hue values outside the effective temperature sensitivity range are almost constant and do not impose poorly predicted temperatures. Temperature regions outside the sensitivity range can be reliably detected because of the significantly reduced intensities. The data points in Fig. 6 can be represented by the polynomial:

$$\frac{T_{poly}}{^\circ C} = \sum_{\eta=0}^{8} C_\eta \cdot \langle H_{kl} \rangle_k^\eta \ , \tag{8}$$

with the coefficients summarized in Table 4. Using this explicit expression, the fluid temperature can be calculated from locally obtained hues. Conditions of applicability are:

- The TLC formulation BM/R35C20 W is considered.
- A digital camera with NTSC color filters and a WB of 5600 K is used.
- The color temperature of the light source matches that of the WB of the camera.
- The angle $\phi = 90$ °.
- The temperature interval T:[$T_{1,W} = 33.77$ °C, $T_{2,W} = 35.09$ °C].

For a confidence interval of 95.4%, the uncertainty of the hue angle δH_l can be calculated from the data plotted in Fig. 6 (Moffat 1988):

$$\delta H_l = 2 \left[\frac{1}{m-1} \sum_{k=1}^{m} \left(H_{kl} - \langle H_{kl} \rangle_k \right) \right]^{0.5} \ , \tag{9}$$

where $\langle H_{kl} \rangle_k$ denotes a line-average (x-direction). If the polynomial in (8) is used, the uncertainty of the temperature prediction follows to:

$$\delta T = \frac{dT_{poly}}{dH} \delta H_l \ . \tag{10}$$

The result is shown in Fig. 7, a reversed plot of Fig. 6. Between the temperature levels $T_{1,W}$ and $T_{2,W}$, (8) is

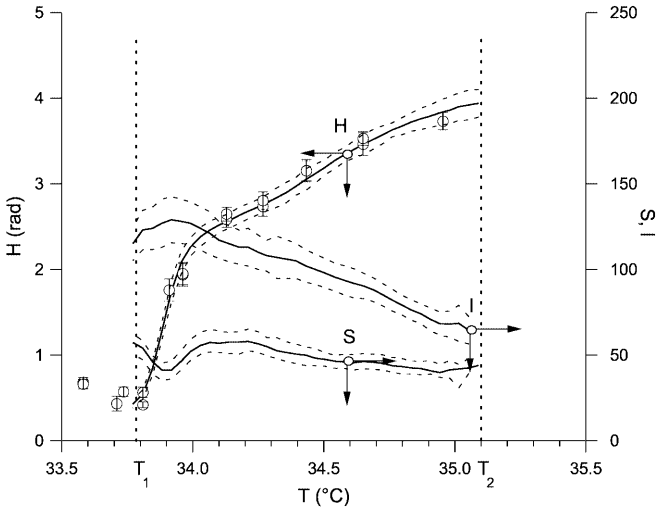

Fig. 6. Hue, saturation, and intensity versus the fluid temperature from a measurement in a thermally stratified layer in deionized water for $\phi = 90°$ (confidence interval: 95.4%). Measurements from constant temperature fields are included

Table 4. Coefficients C_η of the eighth-order polynomial

C_0	31.9194	C_3	33.6841	C_6	−2.6206
C_1	11.1639	C_4	−24.4564	C_7	0.350746
C_2	−26.6679	C_5	10.4994	C_8	−0.0194357

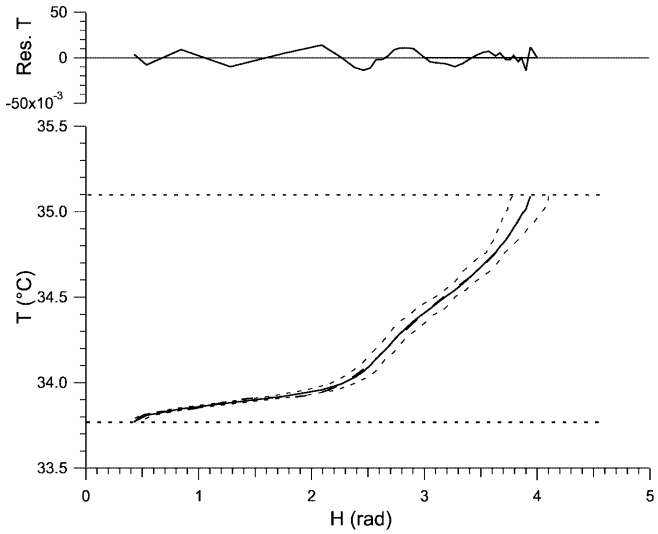

Fig. 7. Measured temperature (thermally stratified layer) and prediction of the temperature fit versus H. Residuals for the polynomial regression are shown (*top*)

included in the plot, together with the residuals for the polynomial regression.

We now use the measurements in a thermally stratified layer of deionized water to estimate the particle density ρ_P from transient images of the settling particles:

$$\varrho_p = \varrho \cdot \left(1 + \frac{18 u_s \nu}{d_p^2 g}\right) \quad . \tag{11}$$

Images with a temporal separation of 4 s are locally cross-correlated (spot size 32×32, $m = n = 40$). The obtained spatial average of the settling velocity u_s in the image plane is 2.13×10^{-5} m/s with a standard deviation of 1.54×10^{-6} m/s. For the mean temperature in the image plane, 34.46 °C, the kinematic viscosity of water is $0.7473 \times 10^{-6} \pm 0.23 \times 10^{-8}$ m^2/s. With Eq. (11) and the gravitational acceleration g, the particle density can be estimated as 1072 kg/m^3. The different influences are:

- the standard deviation of the measured settling velocity $\Delta\varrho_p\varrho_p|_u = 0.02\%$;
- the viscosity variation in the fluid layer $\Delta\varrho_p\varrho_p|_\nu = 0.50\%$;
- the nonuniform particle size distribution $\Delta\varrho_p\varrho_p|_{d_p} = 5.51\%$.

For the considered sample it can be concluded that the measured average particle density was found to be larger than commonly referred to value of 1020 kg/m^3. The relatively broad diameter distribution was found to be the most significant influence for estimating the particle density from sedimentation measurements.

4.2
Uniform temperature fields

For the measurements in uniform temperature fields, only one constant-temperature water bath is used. This bath is connected to both heat exchangers at the bottom and the top wall. The magnetic stirrer inside the cavity is now continuously operated to ensure homogeneous temperature fields within the image plane. Images are taken after steady-state conditions are reached, for water typically after 20 min. Following the procedures explained in Sect. 3, H_{kl} can be locally calculated from the RGB intensities. In Fig. 6 the measured hues obtained in uniform temperature fields are compared with the results from the linear profile. The measurements are consistent with the results obtained in a thermally stratified layer and confirm the validity of Eq. (8). Note that accurately resolving the steep gradient of the calibration curve in Fig. 6 from measurements in uniform temperature fields is much more challenging. A very well mixed fluid is required in the AOV, since minor temperature differences result in significant variations of the locally evaluated hues.

5
Role of experimental parameters

To obtain quantitative temperature information from fluid-dispersed encapsulated TLC particles, not only must a sufficient optical resolution as described in the previous section be used, but the effective temperature sensitivity range must also be considered. The effective temperature sensitivity range of the liquid crystal formulation is an important experimental parameter. First, we discuss the influence of the working fluid in Sect 5.1 and compare the results obtained for glycerol to those obtained for deionized water. Whereas in the previous section a fixed angle ϕ of 90° was considered, here we examine the influence of the angle ϕ on the temperature calibration, see Sect. 5.2.

5.1
Fluid properties

To study how the calibration is affected by different refractive indices of the fluid, see Fig. 8, measurements with water and glycerol are compared at a fixed angular position ϕ of 90°. Figure 8 suggests that the start of the temperature sensitivity is significantly different for the two fluids. The low end of the temperature sensitivity range

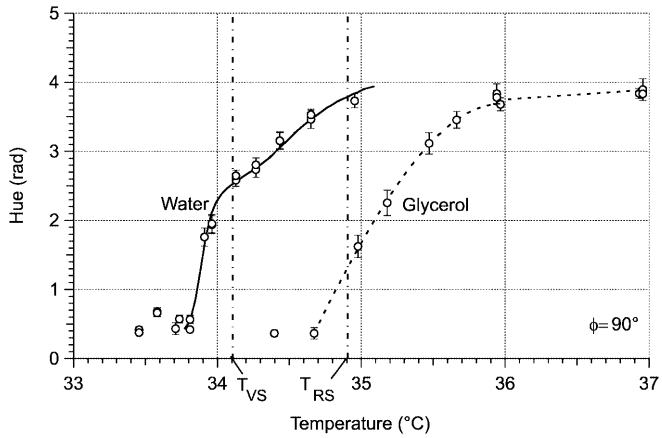

Fig. 8. Influence of the working fluid on the calibration for isothermal measurements in deionized water and glycerol for $\phi = 90°$ (confidence interval: 95.4%). Visible start T_{VS} and red start T_{RS} temperatures reported by Hallcrest (1999) are included for comparison

is $T_{1,W} = 33.77$ °C for water, and $T_{1,G} = 34.70$ °C for glycerol. In addition, the shapes of the two calibration curves are different. For glycerol, a more linear behavior is obtained than for deionized water. Calibration is therefore strongly dependent on the optical properties of the working fluid.

A variation of the fluid properties is of potential interest for measurements in turbulent flows with large temporal scales, namely for natural convection problems. Since the particle density is slightly larger than the density of water, settling can be prevented at the considered mean temperature of 35 °C in an aqueous solution with approximately 11 wt% glycerol. Figure 9 shows the fluid density ρ the kinematic viscosity v, and refractive index n of aqueous glycerol solutions with different mass fractions of glycerol (D'Ans et al. 1977). However, for homogeneous mixtures of fluids with different optical properties, it is important that density stratifications can be neglected for the considered flow fields, since they would result in local color changes and make an accurate reconstruction of the temperature impossible. A calibration for homogeneous mixtures of working fluids with different refractive indices and densities can therefore not be done in a stratified layer. Furthermore, quantitative LCT measurements are not applicable to double-diffusive convection.

5.2 Angle of observation

The experimental set-up shown in Fig. 3 allows the angle between the light-sheet plane and the camera axis ϕ to be varied. The light sheet crosses the volume spanned by the cameras AOV and the telecentric range of the objective δ_{tel}. Since a telecentric objective is used, the obtained images are not only sharp but also distortion free. Glycerol is considered as the working fluid. For the considered

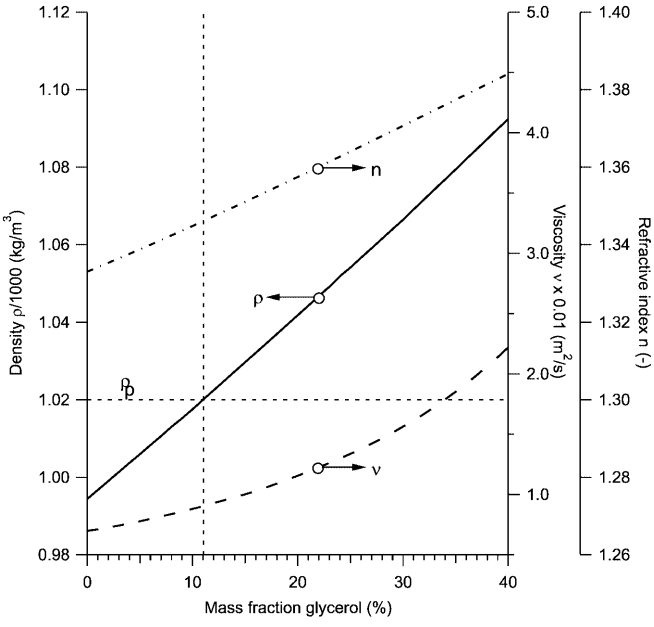

Fig. 9. Fluid density ρ, kinematic viscosity v, and refractive index n of aqueous glycerol solutions as a function of the glycerol mass fraction

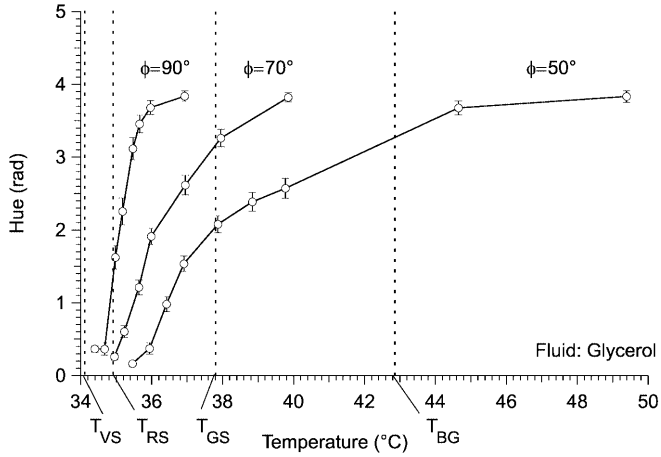

Fig. 10. Influence of the angle ϕ between the camera axis and the light-sheet plane on the color response obtained from isothermal measurements in glycerol (confidence interval: 95.4%). Visible start T_{VS}, red start T_{RS}, green start T_{GS}, and bright green T_{BG} temperatures reported by Hallcrest (1999) are included for comparison

liquid crystal formulation (Hallcrest BM/R35C20), Hallcrest specifies the following characteristic temperatures: visible start, $T_{VS} = 34.1$ °C; the red start, $T_{RS} = 34.9$ °C; the green start, $T_{GS} = 37.8$ °C; the bright green, $T_{BG} = 42.8$ °C; the blue start, $T_{BS} = 55.8$ °C; and the upper colorless limit, $T_{CL} = 68.0$ °C. Three angular positions ϕ equal to 50°, 70°, and 90° are considered. The obtained results are shown in Fig. 10 and indicate a strong dependence of the color angle H on ϕ. For decreasing ϕ, a slight increase in the start and a significant increase in the width of the larger temperature range are observed. Most important, the obtained results connect the calibration conducted in a 90° configuration with the nominal temperature sensitivity range $\phi \rightarrow 0$ provided by Hallcrest (1999). The angular dependence of the calibration is relevant to applications where a Scheimpflug configuration is used, e.g. for combining the liquid crystal thermometry technique with stereoscopic PIV.

6 Summary

The accurate relation of the color response from TLC particles, which are suspended in a working fluid, has been systematically studied for glycerol and deionized water. A 3-chip progressive scan RGB camera equipped with a telecentric measuring objective is used for image formation.

Calibration is conducted for both a uniform temperature field and a linear temperature profile. Care has been taken that particle images are represented by more than one pixel and that saturated pixels (pixel overflow) are avoided. Consistent with literature findings, the calibration curve obtained for $\phi = 90°$ in deionized water shows an effective temperature sensitivity range that is significantly smaller (approximately 7%) than its nominal value. Since the temperature sensitivity range of commercially available TLC formulations is usually specified for $\phi \rightarrow 0$, such knowledge is necessary to properly select a TLC formulation for the considered measurement application, i.e.

temperature field. The results obtained for constant temperature fields and thermally stratified layers show very good agreement. From measurements in a thermally stratified layer of water, the average particle density was estimated to be 1072 kg/m^3, a value larger than the one used in most references. When comparing the results that are obtained for glycerol and de-ionized water, a similar width of the effective temperature sensitivity range is found. However, the start temperature for glycerol is approximately 0.9 °C higher than for water. The dependence of the calibration on the fluids refractive index suggests that LCT is not applicable to double-diffusive convection for homogeneous mixtures of fluids with different optical properties. The width of the effective temperature sensitivity range is found to increase significantly with a decreasing angle ϕ between the light-sheet plane and the optical axis of the camera.

The obtained information allows for the design and performance of reliable simultaneous temperature and velocity measurements for a wider range of transient flow applications and experimental configurations than considered in most present works.

Because of the large effective temperature sensitivity range, combined LIF/PIV techniques are mainly applied to free flows, i.e. natural convection problems, free jets, and free shear layers. Note that even for the considered TLC formulation with the largest commercially available nominal temperature sensitivity range of 20 °C, the effective temperature sensitivity is only 1.32 °C. A combined LCT/PIV technique is therefore particularly advantageous for applications with small spatial variations of the fluid temperature, e.g. for turbulent heat transfer in wall-bounded flows of transparent liquids.

References

Adrian RJ (1995) Limiting resolution of particle image velocimetry for turbulent flow. In: Advances in Turbulence Research–1995, Proc. 2nd Turbulence Research Assoc. Conf., Pohang Inst. Tech., 1–19

Behle M, Schulz K, Leiner W, Fiebig M (1996) Color-based image processing by wide-band liquid crystal thermography. Appl Sci Res 56: 113–143

Dabiri D, Gharib M (1991) Digital particle image thermometry: the method and implementation. Exp Fluids 11: 77–86

Dabiri D, Gharib M (1996) The effects of forced boundary conditions on flow within cubic cavity using digital particle image thermometry and velocimetry. Exp Therm Fluid Sci 13: 349

D'Ans J, Surawski H, Synowietz C (1977) Landolt-Börnstein. Numerical data and functional relationships in science and technology, New Series. Springer-Verlag, Heidelberg New York

Farina DJ, Hacker JM, Moffat RJ, Eaton JK (1994) Illuminant invariant calibration of thermochromic liquid crystal. Exp Therm Fluid Sci 9: 1–12

Günther A, Rudolf von Rohr P (2000) Simultaneous visualization of temperature and velocity fields in turbulent natural convection. In: Proc. 34th National Heat Transfer Conference, Pittsburgh

Günther A (2001) Large-scale structures in Rayleigh–Benard convection and flow over waves. PhD thesis, Swiss Federal Institute of Technology (ETH) Zurich, Diss. ETH No. 14359

Hallcrest (1999) Personal communication

Hay JL, Hollingsworth DK (1998) Calibration of micro-encapsulated liquid crystals using hue angle and a dimensionless temperature. Exp Thermal Fluid Sci 18: 251–257

Kasagi N, Moffat RJ, Hirata M (1989) Liquid crystals. In: Yang WJ (ed) Handbook of flow visualization. Hemisphere, New York, 105–124

Lutjen PM, Clark WM, Prasad V (1999) Liquid crystal thermography and scanning flow tomoscopy for three-dimensional temperature field measurement. In: Proc. 33rd National Heat Transf Conf, Paper NHTC99–215

Moffat RJ (1988) Describing the uncertainties in experimental results. Exp Thermal Fluid Sci. 1: 3–17

Park HG, Dabiri D, Gharib M (2001) Digital particle image velocimetry/thermometry and application to the wake of a heated cylinder. Exp Fluids 30: 327–338

Raffel M, Willert C, Kompenhans J (1998) Particle image velocimetry. A practical guide. Springer, Heidelberg

Sakakibara J, Adrian RJ (1999) Whole field measurement of temperature in water using two-color laser induced fluorescence. Exp Fluids 26: 7–15

Smith CR, Sabatino DR, Praiser TJ (2001) Temperature sensing with thermochromic liquid crystals. Exp Fluids 30: 190–212

Wagner W, Kruse A (1998) Properties of water and steam. The industrial standard IAPWS-IF97 for thermodynamic properties and supplementary equations for other properties. Springer, Berlin